

Article

# Research on Stress Isolation and Precision Enhancement of Resonant Pressure Sensor

Qingtao Mu<sup>1,2</sup>, Kai Shi<sup>2</sup>, Xiaofeng Chen<sup>2</sup>, Fan Zhao<sup>2</sup>, Yulu Han<sup>2</sup>, Hua Liu<sup>2</sup>, Jianbing Xie<sup>1\*</sup>

<sup>1</sup> MOE Key Laboratory of Micro and Nano Systems for Aerospace, School of Mechanical Engineering, Northwestern Polytechnical University, Xi'an 710072, Shaanxi 710000, China

<sup>2</sup> MEMS Division, Shaanxi Huayan Aviation Instrument Company, Xi'an, Shaanxi 710000, China

\* Corresponding author email: [xiejb@nwpu.edu.cn](mailto:xiejb@nwpu.edu.cn)

**Abstract:** Silicon resonant pressure sensors are widely used in aerospace and industry due to their high accuracy, good linearity, and long-term stability. Due to the stress and signal processing limitation, its accuracy is difficult to meet the application requirements, and we can only search methods to approach this continuously. This research introduces a stress-isolated structure and a processing method of frequency signal to enhance the index. The stress-isolated structure separates the press-sensor from the printed circuit board by nested bonding for plates with silica gel. It minimizes the transmitted stress but no affect on the electrical connection. The analysis algorithm of frequency based on a given waveform number instead of a given time improves the analytical accuracy of frequency and pressure. By redesigning the interrupt timing control strategy in Microcontroller unit, it addresses sudden jumps of frequency signal. The proposed technique compared to similar schemes, tested on a resonant pressure sensor at a temperature condition of  $-45\text{ }^{\circ}\text{C}$  to  $75\text{ }^{\circ}\text{C}$  and barometric condition of 3.5 kPa to 110 kPa, reduces the effect of stress effectively, and enhances to 0.01Hz in accuracy of frequency. More importantly there is no sudden jump in frequency signal. The pressure accuracy is increased by 3.5 times to 0.0145% after calibrating. Over-all, the advised method meets the requirement of high accuracy and promotes applications in the aerospace field.

**Keywords:** resonant pressure sensor; stress isolation; frequency resolution; pressure measurement



**Copyright:** © 2024 by the authors. This article is licensed under a Creative Commons Attribution 4.0 International License (CC BY) license (<https://creativecommons.org/licenses/by/4.0/>).

**Citation:** Qingtao Mu, Kai Shi, Xiaofeng Chen, Fan Zhao, Yulu Han, Hua Liu, Jianbing Xie. "Research on Stress Isolation and Precision Enhancement of Resonant Pressure Sensor." *Instrumentation* 11, no.4 (December 2024). <https://doi.org/10.15878/j.instr.202400222>

## 1 Introduction

Pressure sensors are devices that convert pressure signals into electrical signals according to specific rules. Micro electro mechanical System (MEMS) pressure sensors, which are micro pressure sensors based on MEMS technology, can be classified into capacitive<sup>[1,2]</sup>, piezoresistive<sup>[3,4]</sup>, piezoelectric<sup>[5]</sup>, and resonant pressure sensors<sup>[6,7]</sup>. Among these, silicon resonant pressure sensors (RPS) are the most accurate<sup>[8,9]</sup>, compared with capacitive pressure sensors and piezoresistive pressure sensor, the annual stability of silicon resonant pressure

sensors is 0.01%, which is 5 to 10 times that of the former, the measurement accuracy is 0.01%, which is 10 times that of the former. Transistor-Transistor Logic (TTL) square wave signals are easier to get a digital output than analog voltage, shown in Table 1. They are widely used in aerospace, automotive electronics, and biomedicine.

The RPS use single crystal silicon as an elastic body and advanced MEMS technology to process silicon resonant structures on silicon wafers. They employ closed-loop control pressure measurement by detecting the vibration frequency of the sensitive structure in

Table 1 Main performance of different sensors

| performance                      | capacitive press sensor | piezoresistive pressure sensor | resonant pressure sensor |
|----------------------------------|-------------------------|--------------------------------|--------------------------|
| Stability (%/year)               | 0.05~0.1                | 0.1                            | 0.01                     |
| Precision (%FS)                  | 0.1                     | 0.1                            | 0.01                     |
| Resolution (ppm)                 | 10~100                  | 10                             | 10                       |
| Temperature coefficient (ppm/°C) | 4                       | 1600                           | 30                       |
| Output signal                    | voltage                 | voltage                        | frequency                |

response to pressure variations. The main parameters of RPS include measuring range, accuracy, stability, and working temperature, in which the accuracy and stability are affected by temperature stress commonly.

Environmental temperature is a crucial factor affecting pressure sensors. When the ambient temperature changes, the physical properties of the materials change<sup>[10]</sup> and impact the accuracy of the pressure sensors. The thermal stress caused by the thermal expansion coefficient of the materials also results in the temperature drift of the sensors. To improve the accuracy of RPS, the impact of temperature must be minimized. Renata et al.<sup>[11,12]</sup> achieved this by creating a thin layer of SiO<sub>2</sub> on the surface of a silicon (Si) resonator, balancing and counteracting the temperature coefficient of the Young's modulus of silicon, thereby improving the temperature characteristics of the resonator and achieving a frequency variation of less than  $1.2 \times 10^{-6}/^{\circ}\text{C}$ . Li Guangxian et al. designed a low-temperature sensitivity resonant pressure sensor based on a Si-SiO<sub>2</sub> composite H-shaped resonant beam and a dual resonator structure, achieving a lower temperature sensitivity<sup>[13]</sup>. These measures are implemented on the pressure core. In the application of the pressure core, designing a nested bonding stress isolation structure is also an effective measure to reduce the impact of temperature.

By analyzing the mechanism of resonant frequency changes in the support at varying temperatures, it was determined that deformation caused by the characteristics of the carrier material is the main factor causing changes in resonant frequency. To reduce the environmental stress, a structure of nested bonding stress isolation is designed. This structure uses silicone and multi-layer isolation methods to reduce the impact of thermal stress on the pressure sensor.

The output of the sensor, a frequency signal related to pressure, relies on precise frequency analysis for accurate measurement. Frequency analysis typically involves a microprocessor counting frequency signals (TTL square waves) within a specified time range. However, due to the high-frequency resonance characteristics of the core body, occasional frequency errors may occur, leading to frequency jumps during prolonged operation and reduced measurement accuracy.

To solve the problem of frequency jumps, a high-frequency crystal oscillator is used as a reference. We propose a method to determine the resonant frequency

based on the time required for a specific number of frequency signals. By combining Microcontroller Unit (MCU) interrupt timing control, we effectively reduce errors introduced by time-based frequency determination and calculation delays caused by interrupt conflicts, thereby improving the accuracy of frequency signal analysis. By leveraging high-precision frequency signals and applying polynomial compensation, we further enhance the pressure measurement accuracy of the pressure sensor.

## 2 Work Principal of MEMS RPS

The working principle of the resonant pressure sensor is based on the change in the resonant frequency of the support beam of the sensitive body. The sensitive body, acting as a pressure-sensitive film, deforms under external pressure, causing the deformation of the support beam firmly connected to it. This deformation changes the resonant frequency of the beam.

A typical resonant pressure sensor structure, as shown in Figure 1, consists of a support beam, pressure-sensitive film, and signal sensor. One end of the support beam is firmly connected to the sensitive pressure film, while the other end is fixed. The sensitive film and the support beam are sealed in a vacuum. When the pressure on the sensitive film changes, the film deforms and drives the support beam to rotate slightly. This rotation alters the resonant frequency of the support beam, which in turn changes the signal from the signal sensor. By measuring this signal, the change in resonant frequency can be calculated, so the pressure information can be calculated.

When the silicon resonant pressure sensor operates, the silicon resonant structure must be driven to a high-frequency oscillation state by the closed-loop control circuit. The frequency signal is then obtained through the signal extraction circuit. The control circuit block diagram is shown in Figure 2. The AGC (automatic gain control) circuit consists of an amplitude detection circuit and a voltage-controlled gain amplifier. Amplitude detection uses a full-wave rectifier circuit and a low-pass filter circuit to convert the AC signal to a DC signal. This DC signal acts as the negative feedback for the voltage-controlled gain amplifier to regulate the gain and control the amplitude of the silicon resonant structure, ensuring consistent and stable oscillation.

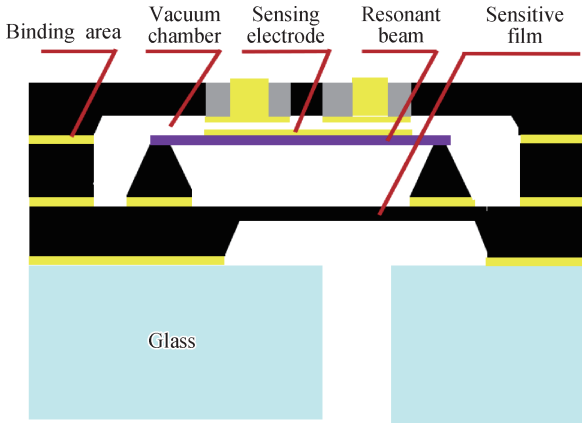


Fig.1 RPS diagram

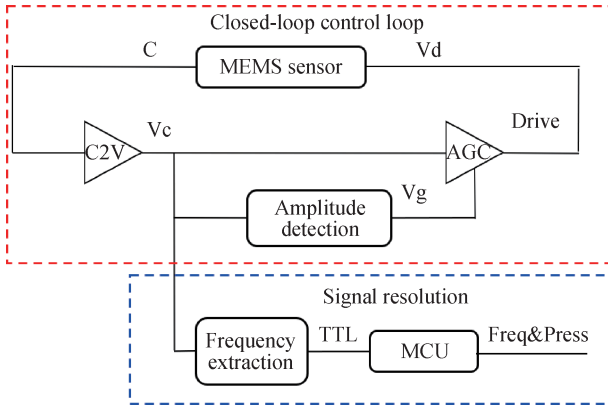


Fig.2 RPS control circuit block diagram

### 3 Thermal Deformation Analysis of Beam

The support beam connected to the pressure-sensitive film is a typical double-ended fixed structure, shown in Figure 3. Suppose  $l, b, h$  are the length, width, and thickness of the beam, respectively. The undamped differential equation according to the elastic theory is:

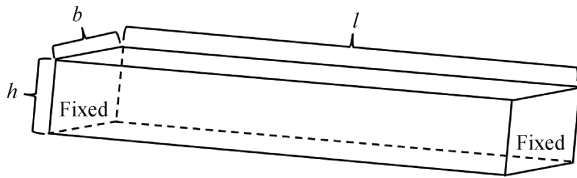


Fig.3 Double-ended fixed beam

$$EI \frac{\partial^4 w(x,t)}{\partial x^4} - \sigma A \frac{\partial^2 w(x,t)}{\partial x^2} = -\rho A \frac{\partial^2 w(x,t)}{\partial x^2} \quad (1)$$

$$A = hb \quad (2)$$

$$I = \frac{hb^3}{12} \quad (3)$$

Solving Eq. (1), when  $\sigma = 0$ , the first-order natural frequency of the support beam is:

$$f_0 = \frac{\alpha_1^2}{2\pi l^2} \sqrt{\frac{EI}{\rho A}} = \frac{4.73^2}{2\pi l^2} \sqrt{\frac{EI}{\rho A}} = 1.028 \sqrt{\frac{E}{\rho}} \cdot \frac{b}{l^2} \quad (4)$$

When  $\sigma \neq 0$ , the first-order natural frequency of the support beam is:

$$f = f_0 \sqrt{1 + \frac{\sigma}{\sigma_c}} \quad (5)$$

$$\sigma_c = \frac{\pi^2 E}{3} \left( \frac{h}{l} \right)^2 \quad (6)$$

In these equations,  $\sigma_c$  is the critical stress,  $E$  is the Young's modulus of the material,  $I$  is the moment of inertia,  $w(x,t)$  is the deflection of the supporting beam,  $A$  is the cross-sectional area of the beam,  $\sigma$  is the axial stress,  $\rho$  is the density,  $\alpha_1$  is the fundamental mode constant,  $\alpha_1 = 4.730$ .

The analysis shows that the resonant frequency of a double-ended beam is only related to the beam length  $l$  and width  $b$ , but not its thickness  $h$ . One step further, the resonant frequency is proportional to the width  $b$  but is inversely proportional to the square of the length  $l$ .

The material of the beam, anchor, and sensitive film in an RPS is always single crystal silicon. They have the same Young's modulus and coefficient of thermal expansion (CTE). In fact, silicon has different material properties at different temperatures<sup>[14]</sup>, as shown in Table 2. The change of CTE causes the length change of silicon.

Table 2 Material properties of silicon at different temperatures

| Temperature (°C) | Young's modulus (GPa) | Density (kgm-3) | Coefficient of thermal(ppm/°C) |
|------------------|-----------------------|-----------------|--------------------------------|
| -153.15(120 K)   | 169                   | 2330            | -0.57                          |
| -73.15(200 K)    | 166.9                 | 2330            | 1.406                          |
| 26.85(300 K)     | 165                   | 2330            | 2.6                            |
| 126.85(400 K)    | 163.1                 | 2327            | 3.253                          |
| 226.85(500 K)    | 163.3                 | 2325            | 3.614                          |

In practical application, the RPS is attached to the carrier with glue, and the material of carrier is Printed Circuit Board (PCB) or ceramic. Usually, CTE of PCB, ceramic and glue are much larger than CTE of single crystal silicon, shown in Table 3, the carrier has a larger transformation than single crystal silicon at the same temperature change. The change of beam under different conditions is shown in Figure 4.

Suppose the pressure is constant,  $l$  is the length of the beam at the temperature  $T_0$ . When the temperature changes from  $T_0$  to  $T_1$ , the length of the beam has a transformation of  $l_{bt}$  due to the properties of silicon material. The resonant frequency of beam is:

$$f_{l_{bt}} = 1.028 \sqrt{\frac{E}{\rho}} \cdot \frac{b}{(l+l_{bt})^2} = \left( \frac{l}{l+l_{bt}} \right)^2 f_0 \quad (7)$$

From Eq. (7), the resonant frequency of the beam changes **indirectly** with temperature. The  $l_{bt}$  is the embodiment of the properties of silicon material itself. Although  $l_{bt}$  is very small ( $l_{bt} \ll l$ ), its effect on the resonant frequency does reduce the accuracy of RPS to a

Table 3 Material properties of different material

| Material                                 | Silicon | Borophosphoric silicon glass | 316L | FR4   |
|--|---------|------------------------------|------|-------|
| Young's Modulus (GPa)                    | 165     | 55                           | 195  | 11    |
| Poisson's ratio                          | 0.28    | 0.25                         | 0.3  | 0.3   |
| Coefficient of thermal expansion(ppm/°C) | 2.6     | 2.8                          | 10.4 | 12-18 |

certain extent. The effect caused by  $l_{bt}$  is the best acceptable state.

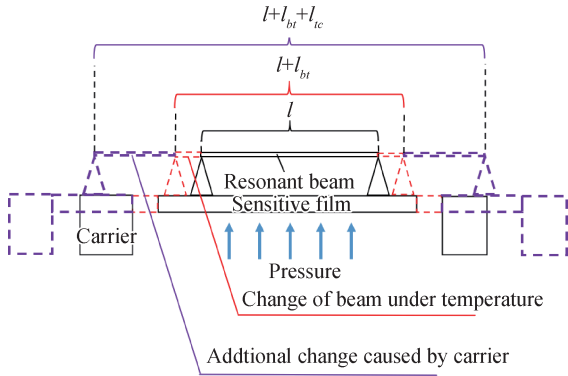


Fig.4 Change of beam under different conditions

Similarly, the length of the carrier has a transformation  $l_{ic}$  at the same temperature change, from  $T_0$  to  $T_1$ . Due to the larger CTE of carriers,  $l_{ic}$  is several times larger than  $l_{bt}(l_{ic}l_{bt})$ . When RPS is attached to the carrier, the length of beam has the same variation. The resonant frequency of the beam at the same temperature change is:

$$f_{l_{ic}} = 1.028 \sqrt{\frac{E}{\rho}} \cdot \frac{b}{(l + l_{bt} + l_{ic})^2} \quad (8)$$

$$f_{l_{ic}} = \left( \frac{l + l_{bt}}{l + l_{bt} + l_{ic}} \right)^2 f_{l_{bt}} = \left( \frac{l}{l + l_{bt} + l_{ic}} \right)^2 f_0 \quad (9)$$

Refer to Eq. (9), it indicates that the resonant frequency of the beam changes under the influence of the deformation of the carrier. The  $l_{ic}$  is the embodiment of the properties of the carrier, and it varies from material to material. The accuracy of frequency will also be significantly reduced by this.  $l_{ic}$  caused by carrier is the biggest disadvantage when improving accuracy, and must find a way to eliminate it.

## 4 Design of Stress-isolated Structure

According to the analysis above, reducing the influence of carrier deformation on the beam is an efficient method to improve the accuracy of PRS. A stress-isolated structure is designed to approach this. A former one is shown in Figure 5. The PRS is bonded to a ceramic plate by silica gel for stress isolation. After testing, this structure is not effective, and cannot meet the accuracy requirements.

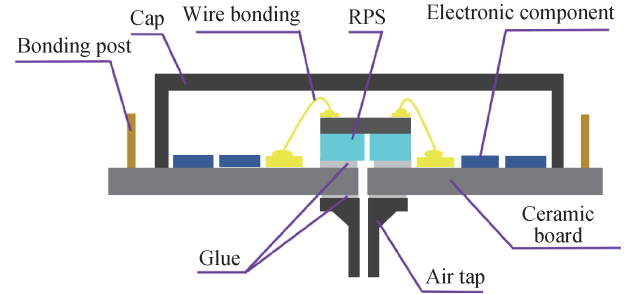


Fig.5 A former stress-isolated structure

In order to improve the situation, A new stress-isolated structure is designed, as shown in Figure 6, the structure includes a cap, binding post, RPS sensor, electronic components, PCB board, isolating plate and air tap.

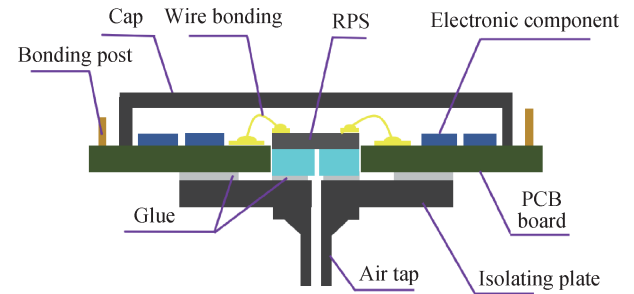


Fig.6 The proposed stress-isolated structure

The electronic components of the close-loop control circuit are soldered to the PCB board, including MCU, temperature sensor, resistance and capacitance. The RPS pads and PCB are bonded with gold wire. An aluminum cap can provide a safe environment for the devices.

Silica gel and nested bonding are the key ways to decrease the impact of the deformation of carrier on RPS. Silica gel is an ideal adhesive due to its good thermal stability, chemical stability, and high mechanical strength. It can work reliably over a wide temperature range ( $-60$  °C to  $200$  °C) and varies little with temperature. The property of electrical insulation has little effect by temperature and frequency. The strong tensile strength can provide sufficient bonding force for the RPS sensor. Nested bonding means that the RPS sensor is glued to the isolating plate, the isolating plate is glued to PCB board and the air tap is glued to the isolating plate. Utilizing nested bonding, the temperature stress of the PCB board and plate can be isolated and absorbed. That is mean,  $l_{ic}$  is very low and has little effect on the resonant frequency of the beam. The RPS sensor is only affected by  $l_{bt}$  when

the temperature changes. Using the compensation algorithm, high precision of RPS can be obtained easily.

## 5 Frequency and Pressure Solving

Frequency is the fundamental signal for atmospheric data calculation, and its accuracy and stability directly affect the accuracy of atmospheric data. The frequency signal acquisition is implemented using STM32F103. The basic principle of frequency measurement is to measure the time  $t$  taken for a certain number of pulses  $N$  and determine the period  $T_1$  of a single pulse to obtain the frequency of the pulse. To meet the frequency acquisition high real-time requirement, the software architecture employs a dual interrupt system to complete frequency

acquisition. Using the counter mode of the STM32 internal timer, the external clock source serves as the timer clock source, and the measured frequency is used as the external clock source input of the timer. During actual measurement, when the counter value of the timer reaches  $N$ , an interrupt is generated, and the value of the count register in the tick timer is read to calculate the time  $t$ .

$$t = T_{SysTick} * \Delta_{sysval} \quad (10)$$

$$f = \frac{1}{T} = N/t \quad (11)$$

where  $T$  is the clock period of the tick timer,  $\Delta_{sysval}$  is the change value of the measured frequency in System-tick during the counting period. The logic diagram of the frequency solving software is shown in Figure 7.

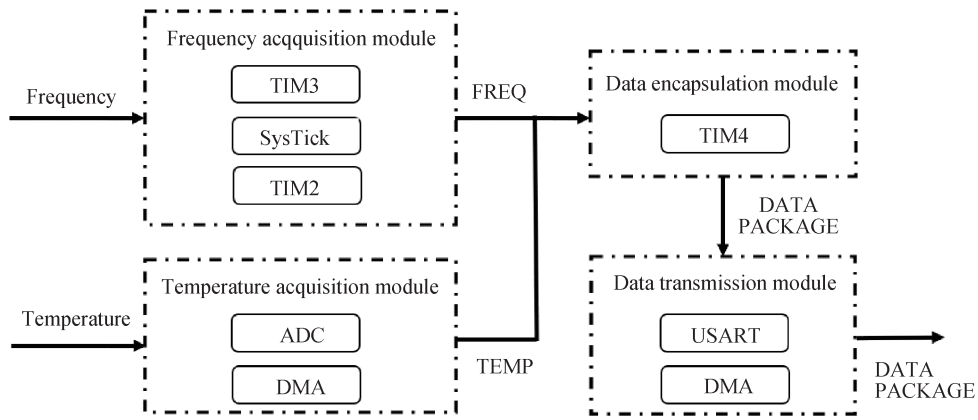


Fig.7 Logic diagram of frequency solving

Multiple sensor frequency signals are managed by counters operating at different frequencies. Although the frequencies of different sensors vary, in practice, there can be instances where different counters trigger simultaneously, causing interrupt competition. This competition can lead to a counter waiting for its interrupt, resulting in a jump in the frequency output. To address this, the frequency analysis algorithm design must include a reasonable timing strategy for interrupts from different counters to avoid competition conflicts. Properly scheduling the timing of interrupts ensures that different functions do not compete for processing time, thus maintaining the accuracy and stability of the frequency output.

The pressure of the silicon resonant pressure sensor is calculated using frequency values under different pressures. By using the frequency values and corresponding temperature values across the full range of temperatures and pressures, the corresponding pressure values can be determined through a polynomial fitting method. The calculation formula can be described as follows:

$$P = p_{00} + p_{10}f + p_{01}t + p_{20}f^2 + p_{11}ft + p_{02}t^2 + p_{30}f^3 + p_{21}f^2t + p_{12}ft^2 \quad (12)$$

where  $P$  is the pressure in kPa,  $f$  is the frequency output in Hz,  $t$  is the temperature output in LSB,  $p_{ij}$  are the coefficients determined by polynomial fitting.

## 6 Experimental Analysis and Discussion

### 6.1 Prototype Manufacturing and Testing

The module of isolated structure can isolate temperature stress effectively, as shown in Figure 8. This structure effectively provides a reliable working environment for the silicon resonant structure.

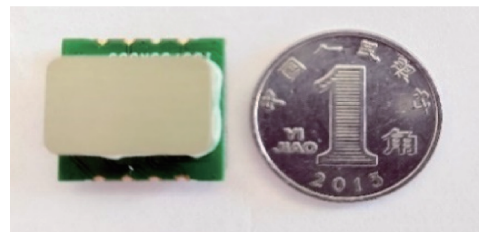


Fig.8 The isolated structure

Utilizing the multi-layer isolation structure and control circuit, a prototype of an atmospheric pressure sensor was manufactured. The prototype is equipped with function of frequency and pressure analysis, Static pressure and full pressure can be measured by two channels respectively. The prototype of atmospheric pressure sensor is shown in Figure 9.

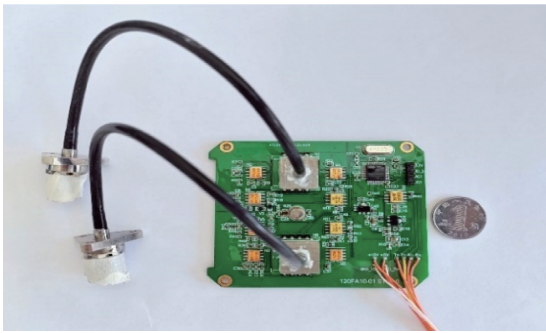


Fig.9 Prototype of pressure sensor

The two channels of signal are shown in Figure 10 and Figure 11 respectively. The result indicates that the square wave signal ranges from 0 to 6V with a 50% duty cycle for two sensors. The frequency of channel 1 is 30.248kHz, while Channel 2 is 30.162kHz. The stable frequency square wave output demonstrates the effectiveness of the closed-loop control circuit.

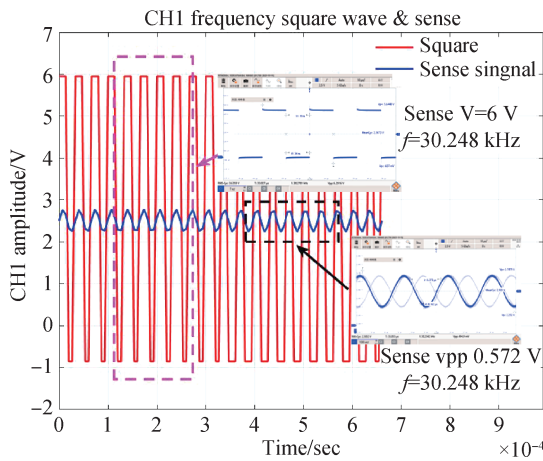


Fig.10 Square & sense output of Chenal 1

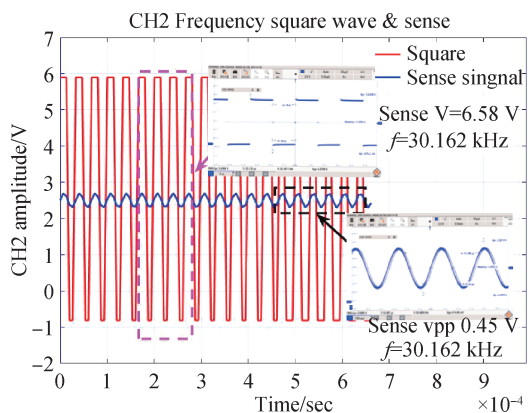


Fig.11 Square & sense output of Chenal 2

### 6.2 Frequency Analysis

Under ambient temperature conditions, the prototype is connected to an atmospheric simulator providing a standard atmospheric pressure input. The stability of frequency analysis during long-term operation is tested. Over 100 seconds, the original frequency algorithm's

output shows the jump in channel 1 and channel 2, with the frequency of channel 1 experiencing a maximum jump of 111.5862 Hz and a standard deviation of 1.66 Hz, and the frequency of channel 2 experiencing a maximum jump of 94.643Hz and a standard deviation of 1.44 Hz, the results are shown in Figure 12 and Figure 13 respectively.

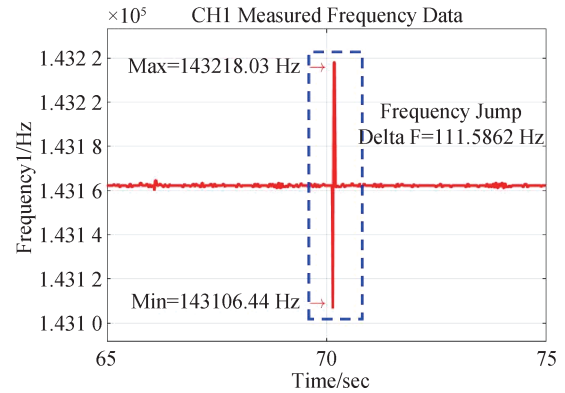


Fig.12 Frequency data analyzed by original algorithm of Chenal 1

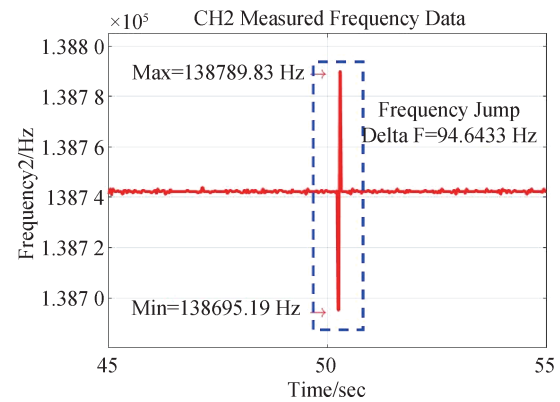


Fig.13 Frequency data analyzed by original algorithm of Chenal 2

After optimizing MCU interrupt timing, the results are shown in Figure 14 and Figure 15. The jump for the frequency of channel 1 is reduced to 0.6905 Hz (peak-to-peak) with a standard deviation of 0.09 Hz, and for the frequency of channel 2, it is reduced to 0.7445 Hz with a standard deviation of 0.1 Hz. The results indicate that the proposed algorithm effectively resolves the issue of

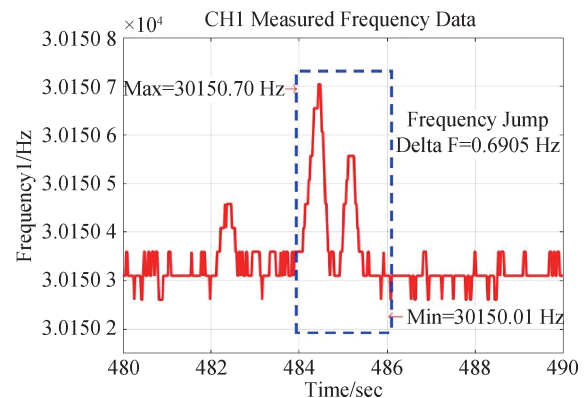


Fig.14 Frequency data analyzed by proposed algorithm of Chenal 1

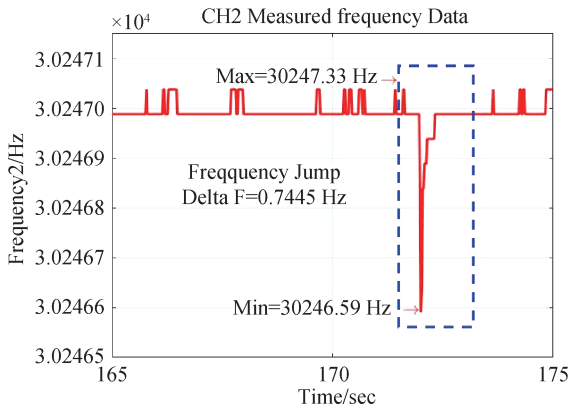


Fig.15 Frequency data analyzed by the proposed algorithm of Chenal 2

frequency analysis errors during long-term operation, ensuring stable frequency output.

Under stable temperature and standard pressure conditions, the output for frequency of channel 1 and channel 2 shows minimal jumps. Frequency of channel 1 has peaks below 0.05 Hz and a standard deviation of 0.01 Hz, shown in Figure 16, whereas frequency of channel 2 has peaks below 0.05 Hz and a standard deviation of 0.02 Hz, shown in Figure 17.

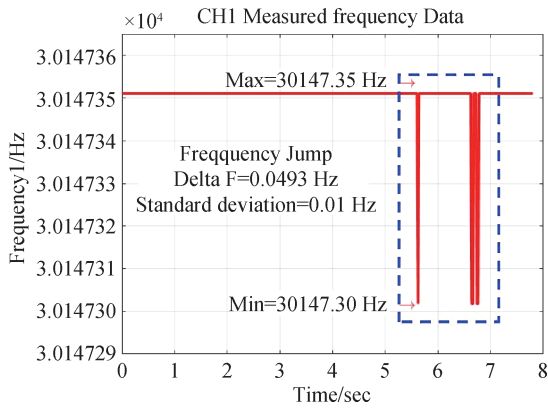


Fig.16 Steady frequency data of Chenal 1

### 6.3 Pressure Analysis

The accuracy of pressure is tested under different temperature ranges and atmospheric pressure conditions.

Table 4 Test pressure point

|                |   |   |    |    |    |    |    |    |    |    |    |    |     |     |
|----------------|---|---|----|----|----|----|----|----|----|----|----|----|-----|-----|
| serial number  | 1 | 2 | 3  | 4  | 5  | 6  | 7  | 8  | 9  | 10 | 11 | 12 | 13  | 14  |
| pressure (kPa) | 4 | 8 | 12 | 16 | 20 | 30 | 40 | 50 | 60 | 70 | 80 | 90 | 100 | 110 |

Table 5 Test temperature point

|                  |     |     |    |    |    |    |    |
|------------------|-----|-----|----|----|----|----|----|
| serial number    | 1   | 2   | 3  | 4  | 5  | 6  | 7  |
| temperature (°C) | -45 | -25 | -5 | 15 | 35 | 55 | 75 |

The max pressure error under the former structure and algorithm across the entire temperature range is 58 Pa, shown in Figure 19. The accuracy of pressure is 0.0527% and cannot meet the requirement.

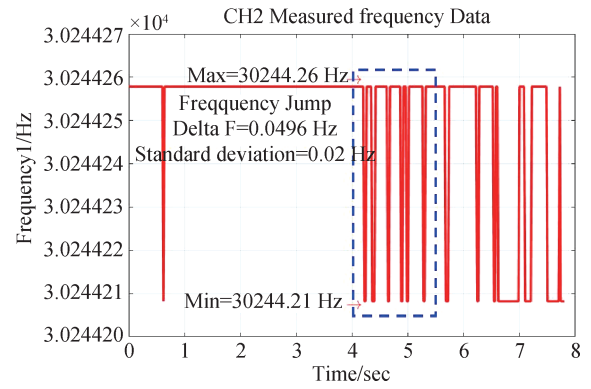


Fig.17 Steady frequency data of Chenal 2

A dedicated atmospheric system is established for testing. The experimental devices include an atmospheric simulator, a high and low-temperature test chamber, a signal converter and a host computer, shown in Figure 18.

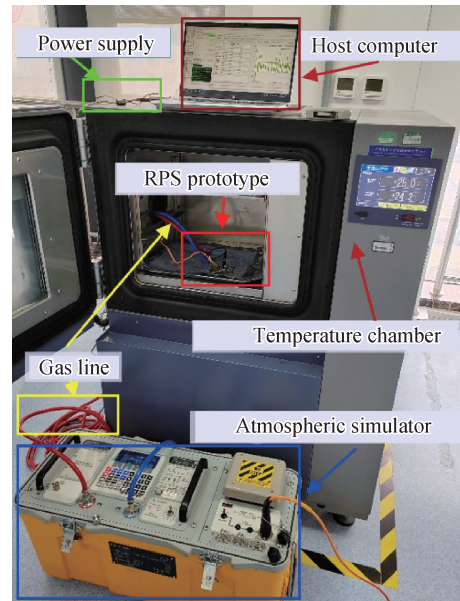


Fig.18 The Dedicated Atmospheric System

The prototype is connected to the atmospheric simulator via a gas pipe to provide standard input pressure. The chosen test points of pressure and temperature are given in Table 4 and Table 5 respectively.

Based on the above frequency test results, pressure analysis is carried out using the specified equation. The pressure error across the entire temperature range is shown in Figure 20. The theoretical maximum error between the output pressure and the standard pressure is 16 Pa, achieving an accuracy of 0.0145%. Pressure accuracy is improved by more than 3.5 times than the former one.

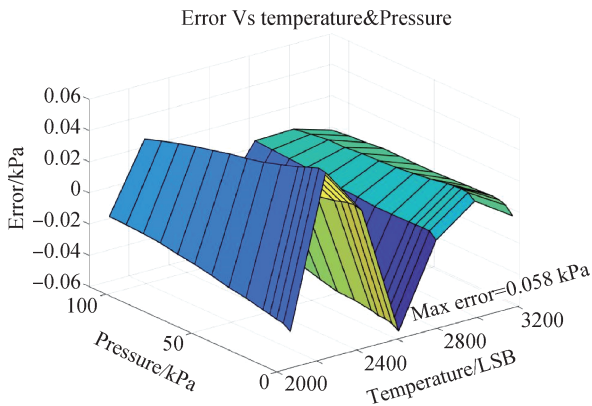


Fig.19 Pressure error under former stress-isolated structure

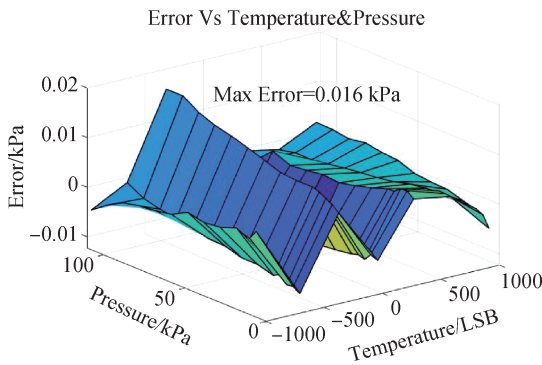


Fig.20 Pressure error under proposed stress-isolated structure

To verify the actual compensation results, we carry out a single point pressure verification under ambient temperature. The atmospheric simulator inputs a 90 kPa standard air pressure signal. The 600 s output signal of the prototype is shown in Figure 21. The actual temperature and frequency data indicate that after the prototype is turned on, although the temperature increases, the frequency signal changes with the temperature, but they all tend to be stable at about 400s. Pressure output is shown in Figure 22.

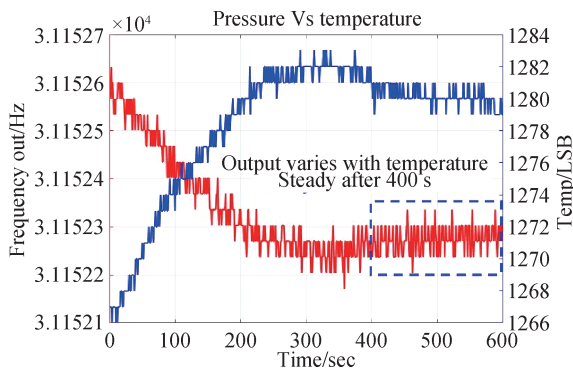


Fig.21 Frequency and temperature data of RPS

According to the results, when a 90 kPa standard air pressure signal is input, we can get a 90.0033 kPa measured to date from the prototype. The maximum error of the pressure is less than 0.0078 kPa and the resolution accuracy is superior to 0.0087%.

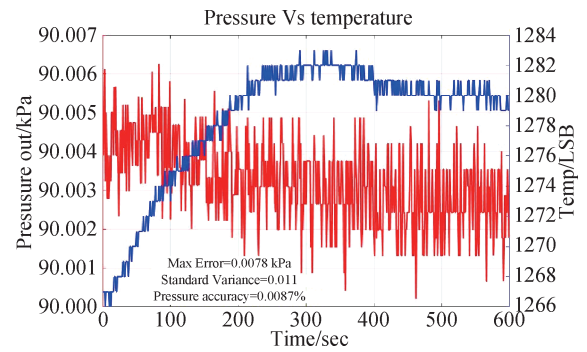


Fig.22 Pressure and temperature data of RPS

## 7 Conclusions

In order to improve the accuracy of RPS, the proposed sensor designs a structure of nested bonding stress isolation. The structure reduces the impact of thermal stress in the working temperature range and helps the sensor achieve high accuracy. The sensor designs a method to determine the resonant frequency based on the time required for a specific number of frequency signals, combining Microcontroller Unit (MCU) interrupt timing control, which can get a high accuracy of frequency signal, thus enhance the pressure measurement accuracy of the sensor. By the test comparison, the pressure calculation accuracy of the sensor is increased from 0.0527% to 0.0145%, and pressure accuracy at 90 kPa reaches 0.0087%. Experimental data show RPS gets a high accuracy of frequency and pressure. The proposed methods above are correct and effective, and can match the requirements of applications in aerospace field.

### Authors Contributions:

The author' contributions are as follows:Qingtao Mu assumed the role of conceptualization and project administration. He made the theoretical analysis of MEMS sensor and designed stress-isolated structure and finished critical test. He mainly wrote the original draft, review and editing. Kai Shi provided methodological guidance and resources for research and experimentation. Xiaofeng Chen, a hardware engineer, was responsible for control circuit design and verification. Fan Zhao, play a key role of software on designing of the algorithm of frequency resolution in MCU. Yulu Han manufactured the prototype of RPS and assisted with experimental analysis. He also charged on formal analysis. Hua Liu charged the data curation of experiment, formal analysis and editing.

### Acknowledgements:

The authors sincerely thanks to senior researcher Xin-Bo Yue of Shaanxi Huayan Aviation Instrument Company for his critical discussion and reading during manuscript preparation.

### Funding Information:

This research received no external funding.

### Data Availability:

The datasets supporting the conclusions of this article are included within the article.

### Conflicts of Interest:

The authors declare no competing interests.

### Dates:

Received 15 August 2024; Accepted 23 October 2024; Published online 31 December 2024

## References

- [1] Sanjeev Kumar Raghuwanshi. (2016). Study of Materials For the Design of MEMS Capacitive Pressure Sensor. *RESEARCH ARTICLE*. APRIL 13.
- [2] Rishabh B. Mishra. (2022). Structural Engineering Approach for Designing Foil-Based Flexible Capacitive Pressure Sensors [J]. *IEEE SENSORS JOURNAL, VOL . 22, NO. 12, JUNE 15*.
- [3] Vinod Belwanshi. (2021). Analytical modeling to estimate the sensitivity of MEMS technology-based piezoresistive pressure sensor. *Journal of Computational Electronics, Vol 20: 668-680*.
- [4] Lu Peng, & Zhang Shunxing. (2022). Design and optimization of new membrane structure for MEMS pressure sensor[J], *Mechanical design, Vol 39(3):61-66*.
- [5] Yonatan Calahorra, Anke Husmann, & Alice Bourdelain. (2019). Highly sensitive piezotronic pressure sensors based on undoped GaAs nanowire ensembles[J], *Journal of Physics D: Applied Physics, Vol 52 294002*.
- [6] Yuan Weizheng, & Ren Sen. (2013). A Review of Silicon Micromachined Resonant Pressure Sensor[J]. *JOURNAL OF MECHANICAL ENGINEERING, Vol 49(20):2-9*.
- [7] LI H, WANG S L, & ZHAO H. (2022). Design and Manufacture of Silicon Resonant Pressure Sensor Based on All Silicon Technology[J]. *Measurement & Control Technology, Vol 41( 9):127-132*.
- [8] X. Du, L. Wang, & A. Li. (2017). High accuracy resonant pressure sensor with balanced-mass DETE resonator and twinborn diaphragms[J]. *Journal of Microelectromechanical Systems, Vol 26(99): 1-11*.
- [9] Ren Sen, Yuan Weizheng, & Deng Jinjun. (2014). Design on electrostatically excited silicon micromachined resonant pressure sensor[J]. *Transducer and Microsystem Technologies, Vol 33(1):64-67,71*.
- [10] Hopcroft M A, Nix W D, & Kenny T W. (2010). What is the Young's modulus of silicon? [J]. *Journal of Microelectromechanical Systems, Vol 19(2):229-238*.
- [11] Melamud R, Chandorkar S A, & Kim B S. (2007). Temperature-compensated high-stability silicon resonators[J]. *Appl Phys Lett, Vol 90(24):244107(1-3)*.
- [12] Melamud R, Kim B S, & Chandorkar S A. (2009). Temperature-insensitive composite micromechanical resonators[J]. *Journal of Microelectromechanical Systems, Vol 18(6):1409-1419*.
- [13] Guangxian Li, & Jing Huang. (2024). Design and Simulation of a Low-Temperature Sensitive Resonant Pressure Sensor[J]. *PIEZOELECTRICS & ACOUSTOOPTICS. Vol 46(2):202-206*.
- [14] Sun Y, Saka M. Thermoelastic damping in micro-scale circular plate resonators[J]. *Journal of Sound & Vibration , 2010, 329(3):328-337*.